The Astrophysical Journal, 961:180 (11pp), 2024 February 1 https://doi.org/10.3847/1538-4357/ad07db

Research on a 44 Day Quasi-periodic Oscillation of Optical Bands for BL Lac S5 0716+714

Lin Lu[1], Bin Sun[1], Zhen-Xing Fang[2], Meng Wan[2], and Yunlu Gong[3]
[1] School of Information, Hunan University of Humanities, Science and Technology, Loudi 417000, People's Republic of China
[2] Department of Physics, Zunyi Normal University, Zunyi, 563002, People's Republic of China
[3] Department of Astronomy, School of Physics and Astronomy, Key Laboratory of Astroparticle Physics of Yunnan Province, Yunnan University, Kunming, 650091, People's Republic of China
Received 2022 November 14; revised 2023 October 24; accepted 2023 October 28; published 2024 January 24

Abstract

By means of astronomical observation data from the 60 cm Telescope at Yunnan Observatory, optical data in the *g*, *r*, and *i* bands were collected for BL Lac S5 0716+714, spanning from 2017 November 10 to 2018 May 15. The original data set contains 21,396 quasi-simultaneous multiband points, with 7132 data points for each band. The Lomb–Scargle periodogram method and the weighted wavelet Z-transform method were used to search for a quasi-periodic oscillation (QPO) signal in the data. For the first time, we report a QPO signal at 44 ± 6 days with a final significance of 3.98σ. Further analysis of the spectrum index reveals that the 44 day QPO signal is most likely explained by a helical motion of a blob with velocity β in the jet, where the viewing angle of the emission region in the jet undergoes periodic variations. In addition, we employed the hypothesis testing method (the null hypothesis) to analyze the flux distribution and determined that a double log-normal distribution provides a better fit; thus, there may be two radiative mini-regions within a jet in this source, so this 44 day QPO signal may be superimposed on a longer-term outburst.

Unified Astronomy Thesaurus concepts: BL Lacertae objects (158); Relativistic jets (1390); Astronomy data analysis (1858); Non-thermal radiation sources (1119)

1. Introduction

Blazars are a subclass of active galactic nuclei (AGNs), with large, rapid, and violent variations across the electromagnetic spectrum. The direction of the jet in blazars points toward Earth (Hong et al. 2018). A supermassive black hole (SMBH) with 10^6–$10^{10} M_\odot$ (in which $M_\odot$ is the solar mass) is contained in its center (Esposito et al. 2015; Gupta et al. 2019). The emission of blazars is dominated by nonthermal radiation (Angel & Stockman 1980; Urry & Padovani 1995; Xiong et al. 2017). According to the strength of the optical emission lines, the blazars are classified into two main subclasses: BL Lacertae objects (BL Lacs) and flat-spectrum radio quasars (FSRQs; Ren et al. 2021a). For FSRQs, the equivalent width (EW) of the emission line is above 5 Å, while for BL Lacs, the EW of the emission line is below 5 Å (Urry & Padovani 1995; Xiong et al. 2017; Hong et al. 2018). The blazar spectral energy distribution (SED) is double peaked. The peaks ranging from X-rays to γ-rays are produced by the inverse Compton (IC) process, whereas the peaks ranging from radio to X-rays are produced by the synchrotron radiation of relativistic electrons within the jet (Ren et al. 2021a, 2021b). According to the location of the SED peak, the blazars are divided into three types: low synchrotron peaked (Lomb–Scargle periodogram (LSP)) ($\nu_{\rm peak} < 10^{14}$Hz), intermediate synchrotron peaked (ISP) (10^{14}Hz $\leqslant \nu_{\rm peak} \leqslant 10^{15}$Hz), and high synchrotron peaked (HSP) ($\nu_{\rm peak} > 10^{15}$Hz) (Abdo et al. 2010; Hong et al. 2017; Iyida et al. 2022).

The variability of the multiband light curves in AGNs allows us to explore their internal structures, physical characteristics, and radiation processes, such as the mass of the central black hole, the radius of the radiation region, and other properties (Urry & Padovani 1995). In particular, the AGNs with quasi-periodic oscillation (QPO) signals may reflect the possible existence of periodic processes within AGNs; the origin of the QPO signal could be caused by a central supermassive binary black hole, such as the most well-known case OJ 287, or reflect the innermost stable orbit of a black hole or the periodic oscillation modes of the accretion disk. However, because of equipment failures, weather conditions, and some errors, the data of the astronomical observations are unevenly sampled over the time interval. Therefore, traditional methods are not suitable for extracting reliable QPO signals from such astronomical data, and with AGN variability being stochastic and dominated by red/flicker noise, searches for QPO signals are fraught with risks and demand high-quality data; thus, a popular topic in time domain astronomy is how to acquire trustworthy QPO signals. To date, the study of the variability of multiband light curves has found QPO timescales ranging from minutes to days, weeks to years, and even decades (Bhatta et al. 2016; Zola et al. 2016; Bhatta 2017). Many physical models have been proposed to explain these QPO signals. For instance, a 2 yr QPO signal was found in the study of the multiband light curve of PG 1553+113 by Ackermann et al. (2015). They discuss several possible physical models that give rise to this QPO signal, such as instability of the pulsational accretion flow with approximating the periodic behavior can explain the modulation of the energy outflow efficiency, non-ballistic hydrodynamic jet precession can explain variations with periods above 1 yr and gravitationally bound supermassive binary black hole systems, the periodic motion of Keplerian orbits may cause periodic accretion perturbations, etc. (Ackermann et al. 2015). For the other blazars, Zhou et al. (2018) studied the γ-ray of PKS 2247-131, and a QPO with a

34.5 day QPO signal of an approximate month-like oscillation was found. To explain the origin of this 34.5 day QPO signal, Zhou et al. (2018) used a helical motion of a blob with velocity β along the jet. Gupta et al. (2009) used wavelet analysis to discover the existence of a 27–73 minute QPO, which was explained by a blob or flare in the inner portion of the accretion disk, and they also obtained the central black hole mass of this source based on these assumptions. The source S5 0716+714 is likely to have IDV-scale QPOs (Gupta et al. 2009). Heidt & Wagner (1996) found a 4 day QPO by the structure function (SF) and autocorrelation analysis methods, and this 4 day QPO may have been caused by a rotating hot spot from the accretion disk. A long QPO signal of 3.3 yr in the optical band was found by Raiteri et al. (2003) and Liu et al. (2012) using the discrete Fourier transform (DFT; Tripathi et al. 2021), the discrete correlation function (DCF; Zhou et al. 2021), and the SF (Rejkuba et al. 2003) methods. Chen et al. (2022) studied the γ-ray band of S5 0716+714 and found a QPO signal of about 31 days, and they used a blob that makes a spiral motion along the jet to explain this QPO signal.

BL Lac S5 0716+714 (with the redshift of $z = 0.31$; Ajello et al. 2020) had been classified as an ISP BL Lac object ($\nu_{\rm peak} = 10^{14.6}$Hz). In this study, we use the LSP and weighted wavelet Z-transform (WWZ) methods to search for the QPO signal of this source and the simulation approach for the light curve to calculate the level of significance of the QPO signal. Thus, using these techniques, a QPO signal of 44 ± 6 days, a month-like oscillation, was discovered for the first time in this source of optical bands. Additionally, the periodic signal with an upward trend shows a complicated radiation mechanism within this source. The use of double logarithms describes well the probability density distribution (PDF) of the original flux of this source, as well as the fact that the spectral indices do not deviate significantly from the mean during the observation. Therefore, we considered it to be an interpretation of a QPO signal with an upward trend with the existence of perhaps two mini-radiative regions within it, one of which produces the 44 day QPO signal, while the other produces a longer flux variation.

Our search for a potential QPO signal of 44 days in the optical bands at *g, r*, and *i* of BL Lac S5 0716+714 with a significance level of 3.98σ is reported for the first time. This paper is organized as follows: in Section 2, the LSP and WWZ methods are introduced; in Section 3, we analyze the light curve of this source using the LSP and WWZ methods, including the estimation of the significance level of the QPO signal, and the presentation of the analytical results; in Section 4, the origin of QPO signal is discussed; and in Section 5, our conclusions are summarized.

2. Method of the Analysis of the Astronomical Data

2.1. LSP Method

The LSP method can correct the phase of periodograms in nonuniform time series (Lomb 1976; Scargle 1982), uncovering QPO signals that may be obscured by noise.

Now it is assumed that there is a group of time series with a nonuniform sampling interval $x(t_j)$, $j = 1, 2, 3.....$, N (VanderPlas 2018; Lu et al. 2023). The following equation gives the LSP power spectral density of the time series. Its fundamental formulation is

$$P_x(\omega_j) = \frac{1}{2}\left\{\frac{\sum_{j=1}^{N}[\{x(t_j) - \bar{x}\}\cos(t_j - \tau)]}{\sum_{j=1}^{N}\cos^2[\omega_j(t_j - \tau)]} + \frac{\sum_{j=1}^{N}[\{x(t_j) - \bar{x}\}\sin(t_j - \tau)]}{\sum_{j=1}^{N}\sin^2[\omega_j(t_j - \tau)]}\right\}, \quad (1)$$

in which f_j is the frequency of the QPO being attempted in units of $1\,\mathrm{day}^{-1}$ (Ren et al. 2021a, 2021b), $P_x(\omega_j)$ is the power spectrum ($(\omega_j = 2\pi f_j)$), $\bar{x} = \frac{1}{N}\sum_{j=1}^{N} x_j$ is the average of time series, N is the number of data points, and τ is the time series phase correction:

$$\tan(2\omega_j\tau) = \frac{\sum_{j=1}^{N}\sin^2(2\omega_j t_j)}{\sum_{j=1}^{N}\cos^2(2\omega_j t_j)}. \quad (2)$$

2.2. WWZ Method

Foster (1996a, 1996b) developed the WWZ method. This method is not only applicable to the analysis of periodic signals of astronomical data but also reflects the variation of periodic signals with time. The time series is projected onto three orthogonal normalized basis vector functions using the WWZ method. These are the three basic vector functions: $\varphi_1(t_i) = 1$, $\varphi_2(t_i) = \cos[\omega_0(t_i - \tau_0)]$, and $\varphi_3(t_i) = \sin[\omega_0(t_i - \tau_0)]$ ($i = 1$, 2, 3...N). A statistical weighting method has been used to adjust for the effects of too dense data in the analysis process, and the expression of the statistical weighting function is $\omega_i = \exp[-c\omega_0^2(t_i - \tau_0)^2]$. The mother function of the WWZ method is the Morlet wavelet (Foster 1996a; Xie et al. 2002). The Z variable of WWZ is defined as follows:

$$Z = \frac{(N_{\rm eff} - 3)V_y}{2(V_x - V_y)}, \quad (3)$$

$$N_{\rm eff} = \frac{\left[\sum\exp(-2c\omega_0^2(t_i - \tau_0)^2\right]^2}{\sum\exp(-2c\omega_0^2(t_i - \tau_0)^2} \quad (4)$$

is the number of valid data points.

$$V_x = \frac{\sum_i \omega_i x^2(t_i)}{\sum_\lambda \omega_\lambda} - \left[\frac{\sum_i \omega_i x(t_i)}{\sum_\lambda \omega_\lambda}\right]^2,$$
$$V_y = \frac{\sum_i \omega_i y^2(t_i)}{\sum_\lambda \omega_\lambda} - \left[\frac{\sum_i \omega_i y(t_i)}{\sum_\lambda \omega_\lambda}\right]^2 \quad (5)$$

are the simulation functions and weighted variables, respectively (Foster 1996a; Zhang et al. 2017).

3. Search for the QPO Signal

We collected optical *g,r*, and *i* band data for S5 0716+714 using data from previously reported literature (Xiong et al. 2020). Considering the Galactic extinction $A_B = 0.102$, $A_R = 0.071$, and $A_I = 0.053$ (Xiong et al. 2020) and by means of the equation $F = (3631 \times 10^{-0.4\cdot\mathrm{mag}}) \times 1000$ mJy, in which 3631 is the zero-point flux density and mag is the magnitudes (Xiong et al. 2020), we obtain the flux. First, we utilized the LSP method to search for periodic signals in the original optical light curves, obtaining peak power values of 631, 665.4, and 680.8 at frequencies of 0.0231, 0.0231, and 0.0234 ($1\,\mathrm{day}^{-1}$)

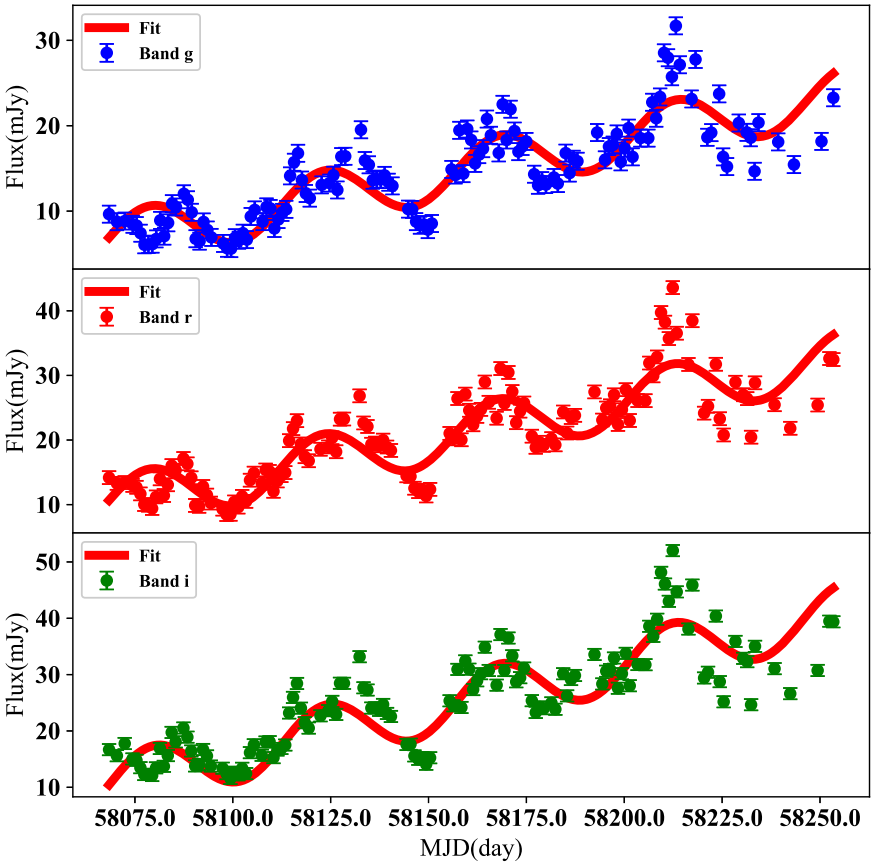

Figure 1. The light curve of BL Lac S5 0716+714 from 2017 November 10 to 2018 May 15. The scatter points denote the original data; the red lines indicate the trigonometric function with a linear trend component, and a potential QPO frequency is about $f = 0.0224(1\ \mathrm{day}^{-1})$.

for the g,r and i bands, respectively. The false-alarm probability (FAP) of the periodic signal is given by the equation $\mathrm{FAP} = 1 - (1 - P)^N$, where N is the number of independent frequencies in the frequency range (i.e., trial factor) and calculated from $(f_{\max} - f_{\min})/\delta f$. Since this is nonuniform sampling data, here we set $f_{\max} \simeq 1/(10\ \mathrm{days})$ and $f_{\min} \simeq 1/(100\ \mathrm{days})$. Because we collect observations at a maximum interval of 7 days, here we set the maximum frequency to 0.1 $(1\ \mathrm{day}^{-1})$, and 100 days is approximately half of the total span of the observation (i.e., 186 days), and δf is the frequency resolution, determined by the total span of the observation. Thus, the number of independent frequencies N is 17 (Horne & Baliunas 1986; VanderPlas 2018; Zhang & Wang 2022). From the results given by the LSP method, we can adopt $P = N_0 e^{-p_0}$ (where N_0 is the number of data points and p_0 is the power of QPO signal); therefore, g: $\mathrm{FAP} = 1 - (1 - 7132 \cdot e^{-631})^{17}$, r: $\mathrm{FAP} = 1 - (1 - 7132 \cdot e^{-665.4})^{17}$, and i: $\mathrm{FAP} = 1 - (1 - 7132 \cdot e^{-680.8})^{17}$. However, it should be emphasized that the adopted FAP method is based on the assumption of white noise, and in the study these data are from AGN, which are actually affected by noise correlations rather than strictly white noise. Therefore, we must treat the results of these FAP estimates with caution and use them here only as preliminary reference values for the estimation of the significance. As a result, for a more precise determination of the significance of the QPO signal, we will employ Monte Carlo simulations for further analysis (Vio et al. 2010; VanderPlas 2018). Due to the large number of original data points and computational resource limitations, we performed a 1 day averaged bin on the original data. As shown in Figure 1, the light curve of the optical bands contains a total number of 132 data points for each band. A periodic signal with a linear upward trend is clearly shown. Thus, we employ the trigonometric function with a linear trend component to fit the data, that is $y(t_i) = A\sin(2\pi f t_i - \theta) + B\cos(2\pi f t_i - \theta) + \alpha t_i + \beta$, in which A, B, f, θ, α, and β are the fitting parameters, $y(t_i)$ is the flux at time t_i, and especially $f(1\ \mathrm{day}^{-1})$ represents the frequency at which potential QPO signals appear, and here we take MJD = 58067 as the start time for the fitting. In addition, in order to quantify the magnitude of the light curve variability, we use the fractional variability amplitude F_{var} and its error $\sigma_{F_{\mathrm{var}}}$ are calculated as (Edelson et al. 2002; Vaughan et al. 2003; Aleksić et al. 2015)

$$F_{\mathrm{var}} = \sqrt{\frac{S^2 - \langle\sigma_{\mathrm{err}}^2\rangle}{\langle \mathrm{flux}\rangle^2}}, \tag{6}$$

and

$$\sigma_{F_{\mathrm{var}}} = \frac{1}{F_{\mathrm{var}}}\sqrt{\frac{1}{2N}}\frac{S^2}{\langle \mathrm{flux}\rangle^2}, \tag{7}$$

where S^2 is the sample variance, $\langle\sigma_{\mathrm{err}}^2\rangle$ the mean square uncertainty, $\langle \mathrm{flux}\rangle$ the average of the fluxes, and N indicates the total number of data points (Li et al. 2021). As shown in Table 1, both the flux amplitude and average flux increase toward lower frequencies for the source. Furthermore, the results of the F_{var} from the original light curves at the g, r, and i bands are also shown in Table 2. However, a power-law dependence of F_{var} with the separated energy bands follows the

Table 1
Results of the Fitting of the PSD in the Optical Bands

Band	K	$\alpha_{\rm low}$	$\alpha_{\rm high}$	$f_{\rm bend}$ (1 day^{-1})	c
g	0.0216 ± 0.0261	1.000 ± 0.693	2.517 ± 0.529	0.0187 ± 0.0239	0.00129 ± 0.0007
r	0.0193 ± 0.023	1.0000 ± 0.58	2.514 ± 0.479	0.0182 ± 0.0223	0.00114 ± 0.00056
i	0.0158 ± 0.0144	1.0000 ± 0.484	2.931 ± 0.65	0.0248 ± 0.020	0.00163 ± 0.0005

Note.
The parameters, K, $\alpha_{\rm low}$, $\alpha_{\rm high}$, $f_{\rm bend}$, and c are the fitted parameters of the PSD.

Table 2
Results of the Analysis of the Flux Variability in the Optical Bands

Band	ΔF(mJy)	$F_{\rm var}$ (%)	Average Flux (mJy)
g	26.1	39.1 ± 2.4	14.3
r	35.1	36.5 ± 2.2	20.6
i	40.4	35.7 ± 2.2	25.2

Notes. The flux amplitude ΔF(mJy) represents the difference between the maximum and minimum values of the flux on the different bands. The fractional variability amplitude $F_{\rm var}$ shows the variation of the optical band during the observation. The average flux is the mean of the optical bands during the observation.

trend of $F_{\rm var}(E) \sim E^{0.2\pm0.046}$, indicating an increasing trend toward higher frequencies.

3.1. Estimation of the Significance Level

Although the LSP and WWZ methods are widely used for nonuniformly sampled light curves to search for QPO signals, usually the flux variability of blazars shows frequency-dependent noise behavior, so the periodograms are likely to cause spurious periods, which can be mistaken for the true periodic component, especially in the lower frequency region (Vaughan et al. 2003; Vaughan 2005; Li et al. 2021). Thus, a Monte Carlo method was also used to obtain the significance of the LSP and WWZ methods. 100,000 light curves, having the same power spectral density (PSD) and flux distribution, were simulated following the method of Emmanoupoulos (Emmanoulopoulos et al. 2013; Lu et al. 2023).

In order to determine the PSD model for generating the artificial light curves used for the significance estimation mentioned above, while considering the nonuniform sampling of the light curve in order to obtain a reliable estimate of the PSD, we undertook the following steps: first, we applied linear interpolation to the data (Emmanoulopoulos et al. 2013; Ren et al. 2021a; Goyal et al. 2022; Li et al. 2023), transforming it into a light curve with a uniform sampling interval based on 1 day. Subsequently, we employed DFT for the estimation of the PSD from uniformly sampled data points (Vio et al. 2010; VanderPlas 2018; Goyal et al. 2022), and we further modeled the PSD of this interpolated data using Equation (8). Finally, we employed the maximum likelihood estimation method from the `iminuit` method to obtain the corresponding PSD parameters and errors, ensuring the reliability of the results of our estimation (Emmanoulopoulos et al. 2013; Chen et al. 2022). A PSD with both a power law and a bending power law is utilized (Emmanoulopoulos et al. 2013):

$$P(f) = \frac{Kf^{-\alpha_{\rm low}}}{1 + (f/f_{\rm bend})^{\alpha_{\rm high}-\alpha_{\rm low}}} + c, \tag{8}$$

in which $P(f)$ denotes PSD, K is the amplitude of the PSD, f is the frequency in units of 1 day^{-1}, $f_{\rm bend}$ is the bending frequency in units of 1 day^{-1}, $\alpha_{\rm low}$ and $\alpha_{\rm high}$ are the two spectral indices, and c denotes positive Poisson noise (Vaughan 2005; Li et al. 2021; Raiteri et al. 2021). As shown in the top panel of Figure 2, the PSD and the fit of Equation (8) are shown for the optical g, r, and i bands, respectively. It is worth noting that in the above analysis, the interpolation process inevitably introduces correlation between data points. However, when the interval of the data points is not very uniform, the DFT (combined with linear interpolation) method is a suitable choice for characterizing the shape of the PSD (Uttley et al. 2002; Emmanoulopoulos et al. 2013; Goyal et al. 2022).

In order to determine the PDF model for the flux generating the artificial light curves used for the estimation of the significance as mentioned above, first, the Shapiro–Wilk test is used for the original flux because it is the most sensitive at rejecting the null hypothesis of a normal distribution, and we reject the null hypothesis if $p < 0.01$ (Shapiro & Wilk 1965). As shown in Table 3, the fluxes of this source in the optical g, r, and i bands are shown to be in better agreement with the log-normal distribution. Second, we performed maximum likelihood fitting of the PDF of the original data. The Bayesian information criterion (BIC) is used to determine the best-fit model. In this work, we obtain g: a double-peak BIC $= -88$, a single-peak BIC $= -86$; r: a double-peak BIC $= -89.7$, a single-peak BIC $= -85.3$; i: a double-peak BIC $= -93$, and a single-peak BIC $= -86.4$; thus, we finally use the double log-normal distribution as the model for the PDF (Pininti et al. 2023):

$$\begin{aligned}{\rm PDF}(A_0, \mu_0, \sigma_0, A_1, \mu_1, \sigma_1) = {} & \frac{A_0}{\sqrt{2\pi}\sigma_0 x} \\ & \exp\left\{\frac{-[\log(x) - \log(\mu_0)]^2}{2{\sigma_0}^2}\right\} \\ & + \frac{A_1}{\sqrt{2\pi}\sigma_1 x} \\ & \exp\left\{\frac{-[\log(x) - \log(\mu_1)]^2}{2{\sigma_1}^2}\right\},\end{aligned} \tag{9}$$

in which PDF denotes the PDF of the original data, A_0 and A_1 are the amplitudes of the model, μ_0, μ_1, and σ_0, σ_1 show the mean and scale of the model, and x is the original flux. As shown in the bottom panel of Figure 2, the PDF and the fit of Equation (9) are shown for the optical g, r and i bands,

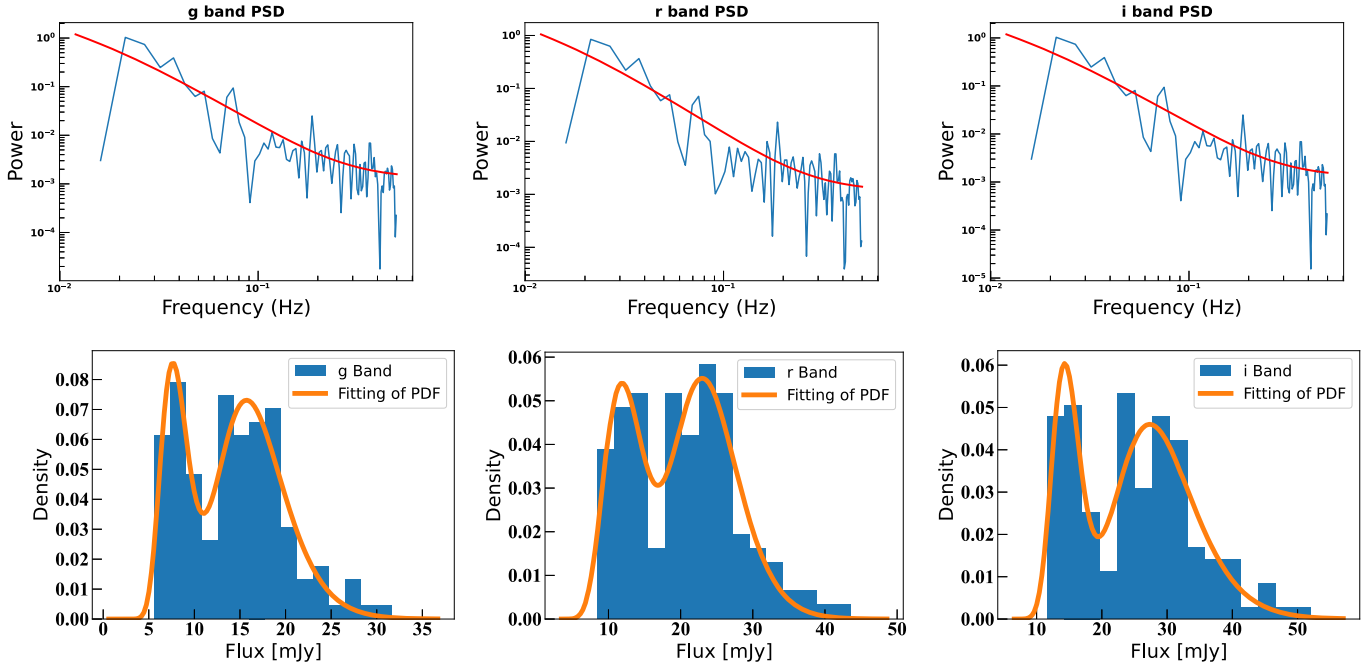

Figure 2. The top panel shows the PSD fit of the original data, and the bottom panel shows the PDF fit of the original flux.

Table 3
Results of the Fitting Results of the PDF in the Optical Bands

Band	A_0	μ_0	σ_0	A_1	μ_1	σ_1	Shapiro–Wilk Test
g	0.073 ± 0.0063	15.74 ± 3.1	0.31 ± 0.048	0.085 ± 0.01	7.62 ± 1.2	0.28 ± 0.034	$P_g = 1.37 \times 10^{-3}$
r	0.054 ± 0.0137	23.19 ± 2.7	0.26 ± 0.044	0.054 ± 0.026	11.87 ± 2.8	0.34 ± 0.17	$P_r = 2.62 \times 10^{-3}$
i	0.046 ± 0.0054	27.36 ± 2.3	0.299 ± 0.02	0.060 ± 0.022	14.28 ± 1.48	0.21 ± 0.063	$P_i = 4.00 \times 10^{-4}$

Notes. The parameters, A_0, A_1, μ_0, μ_1, σ_0, and σ_1 are the fitted parameters of the PDF. The parameters P_g, P_r, and P_i are the results of the Shapiro–Wilk test.

respectively. Based on the analysis above, we obtained the following fitting parameters.

In this fitting, we obtain a goodness of fit of g: $R^2 = 0.5114$, r: $R^2 = 0.6112$, and i: $R^2 = 0.6171$.

Thus, through these simulated light curves with the same PSD and PDF, the PDFs of 100,000 powers at each frequency f_j are computed for the analysis of the results of these 100,000 light curves using a Gaussian kernel. The probability of the PSD x of the simulated light curve above the PSD of the observed data at a certain frequency is $P = Pr\{x > p(f_j)\} = \int_{p(f_j)}^{\infty} \widehat{p}\,(f_j)dx$ (Nilsson et al. 2018; Raiteri et al. 2021); so the significance levels of the QPO signal can be estimated from the analysis of the results of the simulated light curves. The PDF of the original flux may reflect the complicated physical procession of the flux variation within the source (Uttley et al. 2005). A normal flux distribution implies that emission is produced by the linear addition of independent components (Biteau & Giebels 2012); however, a log-normal distribution is produced by multiplying independent components as a reaction chain (Uttley et al. 2005). The flux distribution can be understood as a relation between the jet and accretion disk physics. A log-normal flux distribution is related to fluctuations in the accretion disk at different radii in a scenario outlined by Rieger (2019) and references therein, in which the fluctuation propagates inward to produce an aggregate multiplicative effect in the innermost disk. The jet is then affected by this disruption (Shah et al. 2018). Contrary to the interpretations above, additive processes can also result in a log-normal flow distribution under certain circumstances (Shah et al. 2018). As a result, we consider the possibility that this signal with a periodic upward trend is generated by the superposition of two mini-radiative regions in the jet, one of which has a shorter variation generating this 44 day QPO signal and the other has a longer variation time giving rise to the upward trend (Pininti et al. 2023).

3.2. Analysis of the Results

In Figure 3, the analysis of the results of the LSP and WWZ methods is shown (Zhang et al. 2021). In the right panel, the position at the highest peak is a potential periodic signal in the source, i.e., 0.0226 ($1\ \mathrm{day}^{-1}$), and the corresponding periodic signal is 44 days with a significance level of 4.61σ. In the left panel, a color plot of the WWZ PSD is displayed (yellow is the strongest, and blue is the weakest). Both results are about 44 days and the QPO signal is revealed using these techniques for the first time for the optical bands, and the analysis of the results of the WWZ method also shows that the QPO signal holds steady throughout the observation. Here we further consider this correction in the significance, a final significance is approximately 3.98σ (VanderPlas 2018). Considering the analysis of the results of the LSP, the Gaussian HWHMs at the position of the power peaks provided an uncertainty of 6 days

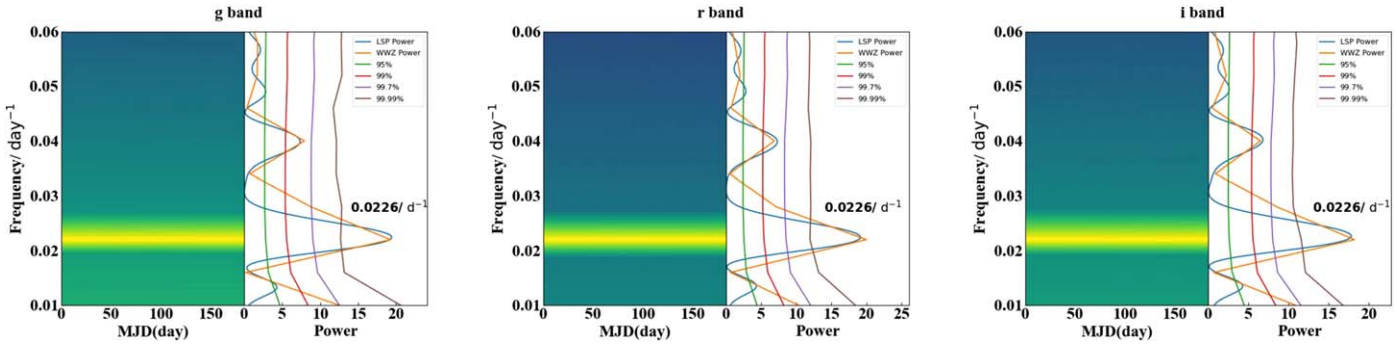

Figure 3. In the left panel, a color plot of the WWZ result is shown (yellow is the strongest, and blue is the weakest). The analysis of the results of the WWZ and LSP methods is shown in the right panel, the coffee color curve represents the significance level of the curve at 99.99%, the purple curve represents the significance level of the curve at 99.7%, the red curve represents the significance level of the curve at 99%, and the green curve represents the significance level of the curve at 95%. The orange curve represents time-averaged WWZ power, and the blue curve represents the LSP power. In the right panel, the highest peak is the position of the periodic signals, which is about 0.0226 (1 day^{-1}), and its counterpart is a 44 day QPO with a significance level of 4.61σ.

in the measurement of the observation period; thus, the final QPO signal should be 44 ± 6 days with a final significance level of 3.98σ. With the results of the LSP analysis, we further estimate the corresponding confidence level using the FAP. We obtain g: FAP $= 6.23 \times 10^{-5}$, r: FAP $= 2.56 \times 10^{-5}$, and i: FAP $= 9.31 \times 10^{-6}$. Thus, the 44 ± 6 day QPO signal is likely to exist in the optical band of S5 0716+714. This is also the first time that these techniques have been used to find an approximate month-like oscillation QPO signal in the optical bands for this source. However, considering that the light curves inherently contain trends, we have conducted a similar analysis process on the detrended light curves in the Appendix.

4. Discussion

In previous studies of the blazar's QPO signals, researchers have detected QPO signals on a range of timescales, from minutes to weeks and even years, across multiple wave bands. The different timescales may be indicative of different underlying physical processes in blazars.

Rani et al. first reported a QPO signal of approximately 15 minutes in the optical band of S5 0716+714, which is one of the fastest QPOs observed in blazars (Rani et al. 2010; Li et al. 2023). In other studies, researchers have also discovered QPO signals of 14 days (Rani et al. 2013), 60–70 days (Ma et al. 2004), and even year-long timescales in the optical band of S5 0716+714, such as the 340 day QPO in the γ-ray reported by Prokhorov & Moraghan (2017) and Bhatta & Dhital (2020), a 3 yr QPO in the optical band found by Raiteri et al. (2003), and recently, a 31 day QPO in the γ-ray discovered by Chen et al. (2022).

Thus, we can see that QPO signals have been observed across multiple bands for the blazar S5 0716+714, which will help reveal interesting physical phenomena and processes internal to blazars. However, we also note that there exist some past studies with likely overestimated significance, primarily due to not considering the analysis of white noise and/or red noise background. For instance, although Prokhorov & Moraghan (2017) reported a 340 day QPO in the Fermi-LAT γ-ray light curve, they neglected to incorporate random red noise variations. Moreover, QPOs on different timescales are unlikely to share the same physical origin and may not even appear simultaneously across bands, indicating the complexity of AGN QPOs. Therefore, we believe any claims of QPOs warrant rigorous verification of the analysis.

Notably, in this study of the optical band for S5 0716+714, we have identified for the first time a 44 day QPO signal with a final significance of 3.98σ, and this QPO signal contains an upward trend. As discussed in the Appendix, when analyzing the detrended light curve, we also found a QPO signal on a similar timescale, providing an interesting case for AGN QPO studies. This suggests that the physical origin of this QPO signal may be different from what has been found before. Considering that S5 0716+714 is a BL Lac object, we first considered the variation from the optical bands caused by the variation inside the jet. When the radiation region encounters a shock/turbulence, it is likely to cause a variation in the light curve. As the PDF in Figure 2 shows, this source of radiation is superimposed by two main components. One of them is perhaps motivated by a more long-term trend of variability. Thus, to investigate the origin of this 44 day QPO signal, the spectral index α_{gri} will be further analyzed. Normally, for nonthermal radiation processes, the frequency ν of the observed band and the observed flux F satisfy a power-law relationship, and the expression is $\log F_\nu = -\alpha_{\rm gri} \log \nu + B$, and α_{gri} is the spectral index, F_ν is the observed flux of the corresponding band, and B is a constant (Xiong et al. 2020). Combining $\nu_B = 6.2 \times 10^{14}$Hz, $\nu_R = 4.8 \times 10^{14}$Hz, and $\nu_I = 3.9 \times 10^{14}$Hz Xiong et al. (2020) observed flux, and the spectral index α_{gri} was obtained.

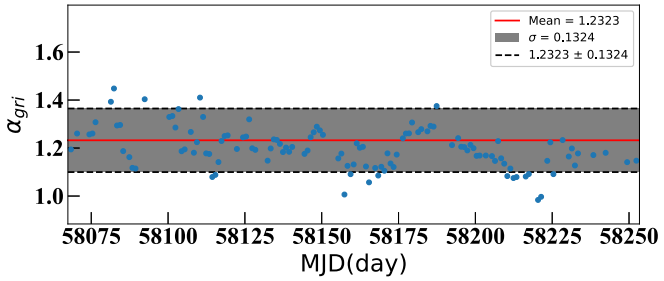

Figure 4. The variation of the spectral index α_{gri} with time is shown here. This result shows that the fluctuations of the spectral indices did not move away from the mean value during the observation.

Since the photon index p in the SED and the spectral index α_{gri} have a linear relationship, the expression is $\alpha_{gri} = \frac{p-1}{2}$ ($N(E) \sim E^{-p}$, $N(E)$ display particle distribution at energy E, and p represents the photon index) (Kapanadze 2021). Therefore, the photon index p also varies without significant fluctuations over the span of the observation.

As shown in the results illustrated in Figures 4 and 5, we believe that the light curves of this source in the g, r, and i

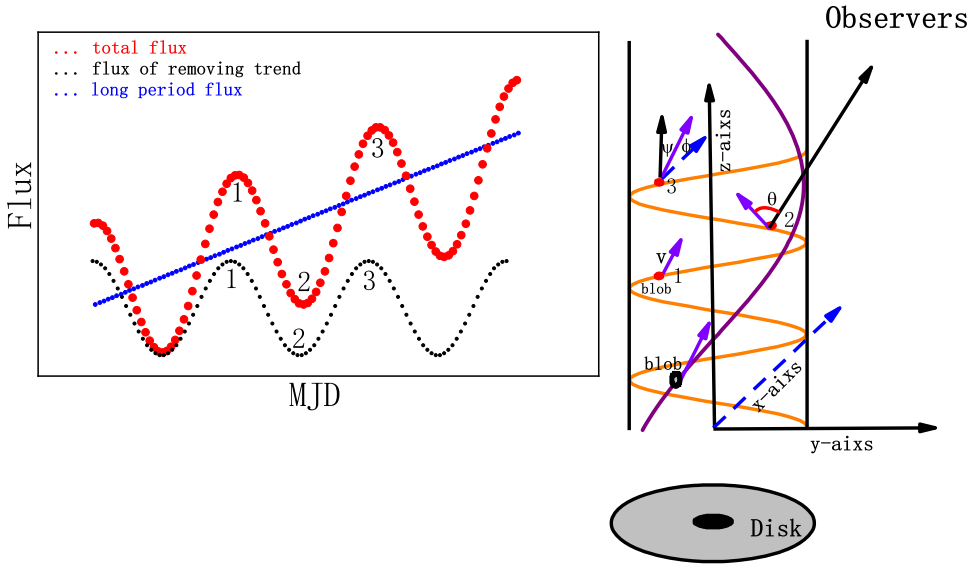

Figure 5. On the left side of Figure 5, the black curve represents the light curve after the trend is removed, the blue curve represents the long-term light curve generated by the precession of the jet over the span of the observation, and the red curve represents the total flux, which is the flux of the long-term QPO superimposed on the flux of the short-term QPO. The red blob produces a 44 day QPO signal, while the black blob produces a long-term flux variation.

bands are likely to have originated from geometric processes within the jet. In Figure 2, we present the PDF of the optical band flux, which follows a double log-normal distribution, so the upward periodic light curve shown in Figure 1 is most likely due to the effect of a month-like oscillation periodic process superimposed on a more long-term geometrical variation process. Here we consider the possibility of two mini-jet components in the jet (Pininti et al. 2023), one of which generates a 44 day QPO signal and the other generates a longer flux with a varying timescale. For a 44 day QPO signal, this can be well explained by a periodic spiral motion of a blob with velocity β along the jet (Camenzind & Krockenberger 1992; Nesci et al. 2005; Zhou et al. 2018). As illustrated in the right-hand panel of Figure 5, we consider a geometric scenario in which the viewing angle θ of an emitting blob motion is a function of time t (Sobacchi et al. 2017). The jet axis is the z-axis, the axis pointing toward the observer and perpendicular to z is the x-axis, and the axis perpendicular to z and x is the y-axis. When the blob is moving with velocity β, the velocity β is decomposed on three axes in the following form (Sobacchi et al. 2017):

$$\overrightarrow{\beta} = \beta(\sin(\phi)\cos(\omega t), \sin(\phi)\sin(\omega t), \cos(\phi)), \quad (10)$$

where ϕ is the angle between the z-axis and ω is the angular velocity of the spiral motion ($\omega = \frac{2\pi}{P_{\rm obs}}$, $P_{\rm obs}$ is the QPO) (Sobacchi et al. 2017; Zhou et al. 2018). The unit vector in the direction of the observer's line of sight is $\overrightarrow{n} = (\sin(\psi), 0, cos(\psi))$, and ψ is the angle between the z-axis and the observer's line of sight. From the analysis above, $\overrightarrow{\beta} \cdot \overrightarrow{n} = \beta\cos(\theta)$ is obtained, so the following formula can be given (Sobacchi et al. 2017):

$$\cos(\theta) = \sin(\psi)sin(\phi)\cos(\omega t) + cos(\psi)\cos(\phi). \quad (11)$$

The relativistic beaming factor is $\delta = 1/[\Gamma(1 - \beta\cos\theta)]$ (Sobacchi et al. 2017), $\Gamma = 1/(1 - \beta^2)^{1/2}$ is the bulk Lorentz factor of the blob, and βc is the speed of motion. For blazars, typical values $\phi = 2°$, $\psi = 5°$, and $\Gamma = 8.5$ can be taken (Zhou et al. 2018). Under the effect of special relativity, a 44 day QPO is much shorter than the real QPO, so by equation $P_{\rm obs} = (1 - \beta\cos(\psi)\cos(\phi))P$ (Zhou et al. 2018), this 44 day QPO is corrected. The corrected quasi-period is $P \approx 10.04$ yr. In the z-direction, the distance that a blob moves in a QPO is approximately $L \approx 3.11$ pc. Through the equation $d_L\left(z\right) = \frac{c}{H_0}(1 + z)\int_0^z [\Omega_\Lambda + \Omega_0(1 + z')^3]^{-1/2} dz'$ (Venters et al. 2009), in which z is the redshift and c is the speed of light, the luminosity distance for S5 0716+714 is further analyzed by us. When $z = 0.31$, d_L is equal to 1612.65 Mpc, it can be seen that this distance is very large and such a large distance makes it impossible to find the spiral motion through very long baseline interferometry (Zhou et al. 2018). Although the analysis suggests that the 44 day QPO of S5 0716+714 is likely to have originated from a spiral motion of a blob along the jet, it still cannot be excluded that it may be due to other causes. For example, the 10.04 yr QPO is obtained after correction, and the timescale of the corrected QPO is close to the timescale of the orbital motion for the binary black hole, which leads us to believe that it could also be generated by the orbital motion of the binary black hole model (Xie et al. 2002; Gupta et al. 2019; Ren et al. 2021a). Gupta et al. (2019) discovered a QPO of about 71 days while studying the γ-ray from the blazar B2 1520+31, and they used a fluctuating hot spot from the innermost stable circular orbit of the accretion disk as an explanation for its origin. So, we cannot exclude that this 44 day QPO may have been generated for the same reason. In addition to the discussion on the origin of the 44 day QPO, we found that there is an upward trend over the span of the observation. The upward linear component is perhaps due to radiation from other parts within the jet, and this part of the radiation region is perhaps also geometrically varying and periodically changing relative to the observer's view, except

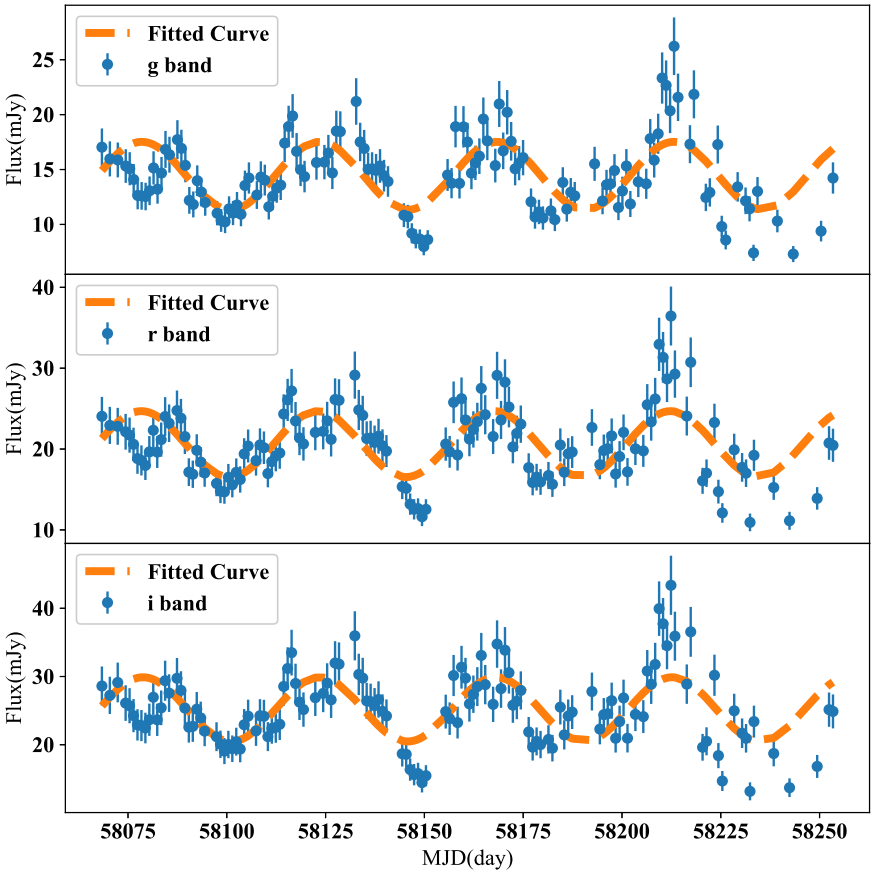

Figure 6. The light curve of BL Lac S5 0716+714 observed from 2017 November 10 to 2018 May 15. The scatter points denote the detrended data; the orange lines indicate the trigonometric function, and a potential QPO frequency is about $f = 0.0224(1\ \mathrm{day}^{-1})$.

that the length of time of this part of the variation is much larger than the part of the 44 day component. The observer may see the phenomenon shown in Figure 1 when the flux in this part of the radiation region with a longer variation time is in a rising state. However, in addition to this explanation, the periodic precession of the jet may also be a reason for the long-term variability. In the left panel of Figure 6, we assume that the long-term QPO is at least larger than our span of observation. And since the entire span of the observation is in an upward phase, we estimate that the long-term QPO is at least 400 days. We have used the sine function $\sin(2\pi t/T)$ to simulate a light curve with a long-term QPO, and T is the estimated long-term QPO. Meanwhile, the sine function is used to model the short-term QPO after excluding the uptrend (Butuzova 2021). When the two parts are superimposed together, they show an upward trend. As shown in Figure 5, we can clearly see that the effect of superposition of the long-term QPO on the short term is almost a linearly upward line over the span of the observation. Therefore, using a linear fit as the rising trend shown in Figure 1 should be a reasonable choice. However, the longer QPO may also come from processes such as accretion disk radiation (Nesci et al. 2005).

5. Conclusions

In this work, we study observational data of the optical *g*, *r*, and *i* bands of BL Lac S5 0716+714. We obtained the following main results:

(1) Using the LSP and the WWZ methods and the simulation method for the light curve, the 44 ± 6 day QPO signal with a final confidence level of 3.98σ is obtained for the first time in the optical band of S5 0716+714. This result also confirms the existence of an approximate month-like oscillation of QPOs in the optical band of blazars.
(2) Based on the analysis of the spectral index α_{gri}, we find that a spiral periodic motion of a blob with velocity β along the jet for this QPO signal is well explained.
(3) According to the analysis above, we find that the use of two mini-radiation regions within the jet may be a good explanation for the light curve of this periodic upward trend. The 44 day QPO signal is produced by one of them, while the longer flux variation is produced by the other. When the long-term variability is in an upward state, a periodic signal with an upward trend may be able to be spotted.

Acknowledgments

This work is partially supported by the regional first-class discipline of the Guizhou province (QJKYF[2018]216), Major research projects for innovation groups in the Guizhou province (grant No. KY[2018]028), Electronic Manufacturing Industry-University-Research Base of Ordinary Colleges and Universities in the Guizhou Province (Qianjiaohe KY Zi [2014] No. 230-3, Youth Foundation of the Education Department of Guizhou Province (No. KY[2017]248) and Guizhou Science and Technology Department(QKHJC[2019]1323) and Talent

base for R&D of new optoelectronic materials and electronic devices.

Appendix

In this appendix, we provide a detailed discussion of the analysis conducted on detrended light curves through quasi-periodic searches. Figure 6 shows the light curve for the removal trend. Removing trends from time series data is a crucial step in ensuring the robustness of our analysis. In the case of the original light curves, we employed a linear trend-fitting procedure involving a combination of trigonometric functions to model and remove the trends (Hong et al. 2018). Therefore, in the process of detrending the light curves, we directly subtracted the corresponding linear trends to obtain detrended light curves. Following the steps in Section 3, we estimate the QPO of the removal trend light curve with 7312 data and the corresponding correction FAP; we obtain g: $\mathrm{FAP} = 1 - (1 - 7132 \cdot e^{-694})^{17}$, r: $\mathrm{FAP} = 1 - (1 - 7132 \cdot e^{-702})^{17}$, and i: $\mathrm{FAP} = 1 - (1 - 7132 \cdot e^{-723})^{17}$, respectively (VanderPlas 2018); these results also show that an extremely high significance for the QPO signal appearing at approximately 44.6 day.

Here we used the same process as in Section 3.1 to estimate the significance of the corresponding QPO, so we still took a 1 day average bin for the light curve of the removal trend here (Hong et al. 2018), and we obtained the data point of 132 after taking bins for the three bands, respectively. Considering the nonuniform sampling of the light curve, in order to obtain a reliable estimate of the PSD, we undertook the following steps: first, we applied linear interpolation to the data, transforming it into a light curve with a uniform sampling interval based on 1 day (Goyal et al. 2022). Subsequently, we employed DFT for the estimation of the PSD from uniformly sampled data points (Emmanoulopoulos et al. 2013; Goyal et al. 2022), and we further modeled the PSD of this interpolated data using Equation (8). Finally, we employed the maximum likelihood estimation method from the `iminuit` method to obtain the corresponding PSD parameters, ensuring the reliability of the results of our estimation (Vaughan 2005; Emmanoulopoulos et al. 2013; Li et al. 2023).

In the fitting in Table 4, we obtained a goodness of fit of g: $R^2 = 0.5917$, r: $R^2 = 0.6171$, and i: $R^2 = 0.592$. Next, we conducted an analysis of the flux distribution of the detrended light curve. Initially, we applied the Shapiro–Wilk test at $p < 0.01$ (Shapiro & Wilk 1965), which revealed that the flux of these detrended light curves follows a normal distribution. Consequently, we contemplated modeling the flux distribution using a normal distribution according to Table 5,

$$\mathrm{PDF}(A, \mu, \sigma) = \frac{A}{\sqrt{2\pi}\,\sigma x} \exp\left\{\frac{-[x - \mu)]^2}{2\sigma^2}\right\}, \tag{12}$$

in which PDF denotes the PDF of the detrended data, A is the amplitude of the model, μ and σ show the mean and scale of the model, and x is the detrended flux. As shown in the bottom panel of Figure 7, the PDF and the fit of Equation (12) are shown for the optical g, r and i bands, respectively.

Here we present the results of the Monte Carlo simulation performed to remove the light curve.

Following the FAP estimation process above, we obtain g: $\mathrm{FAP} = 3.126 \times 10^{-15}$, r: $\mathrm{FAP} = 1.887 \times 10^{-15}$, and i: $\mathrm{FAP} = 4.341 \times 10^{-14}$ for the results of the LSP method. We also consider this correction of the significance for the detrended light curve, and the final significance is approximately 3.48σ based on the result in Figure 8 (VanderPlas 2018; Zhang & Wang 2022). Based on the analysis above, we conclude that there is a QPO signal of approximately 44 ± 6 days present in these three bands.

Table 4
Results of the Fitting of the PSD in the Optical Bands

Band	K	α_{low}	α_{high}	f_{bend} (1 day^{-1})	c
g	0.0203 ± 0.0196	1.000 ± 0.537	2.631 ± 0.514	0.0251 ± 0.0252	0.00128 ± 0.0006
r	0.0178 ± 0.0169	1.0000 ± 0.61	2.692 ± 0.51	0.0247 ± 0.0233	0.00118 ± 0.00049
i	0.0176 ± 0.0161	1.0000 ± 0.561	2.835 ± 0.511	0.025 ± 0.021	0.00141 ± 0.0004

Note. The parameters, K, α_{low}, α_{high}, f_{bend}, and c are the fitted parameters of the PSD.

Table 5
Results of the Fitting of the PDF in the Optical Bands

Band	A	μ	σ	Shapiro–Wilk Test
g	1.481 ± 0.074	13.78 ± 0.024	0.27 ± 0.0133	$P_g = 0.041$
r	1.578 ± 0.082	13.35 ± 0.0225	0.253 ± 0.013	$P_r = 0.028$
i	1.7 ± 0.094	13.11 ± 0.021	0.235 ± 0.013	$P_i = 0.18$

Note. The parameters A, μ, and σ are the fitted parameters of the PDF. The parameters, P_g, P_r, and P_i are the results of the Shapiro–Wilk test.

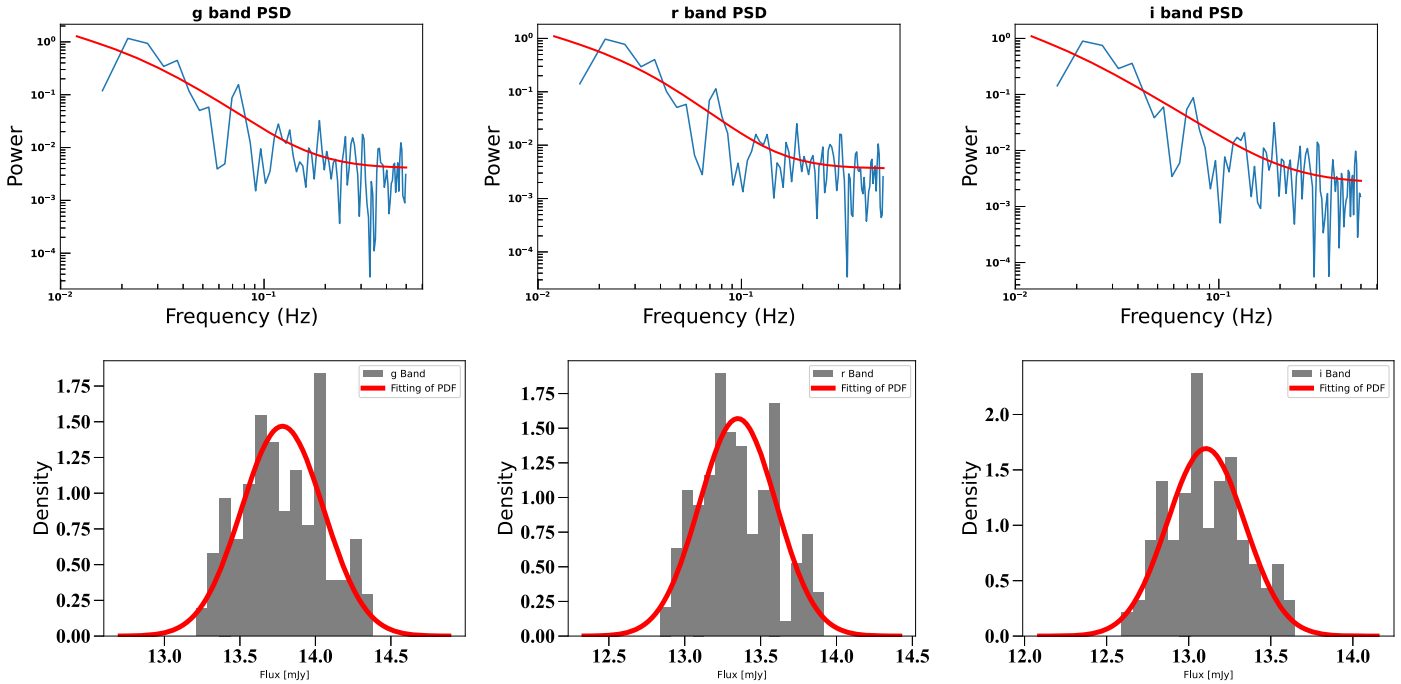

Figure 7. The top panel shows the PSD fit of the detrended data, and the bottom panel shows the PDF fit of the detrended flux.

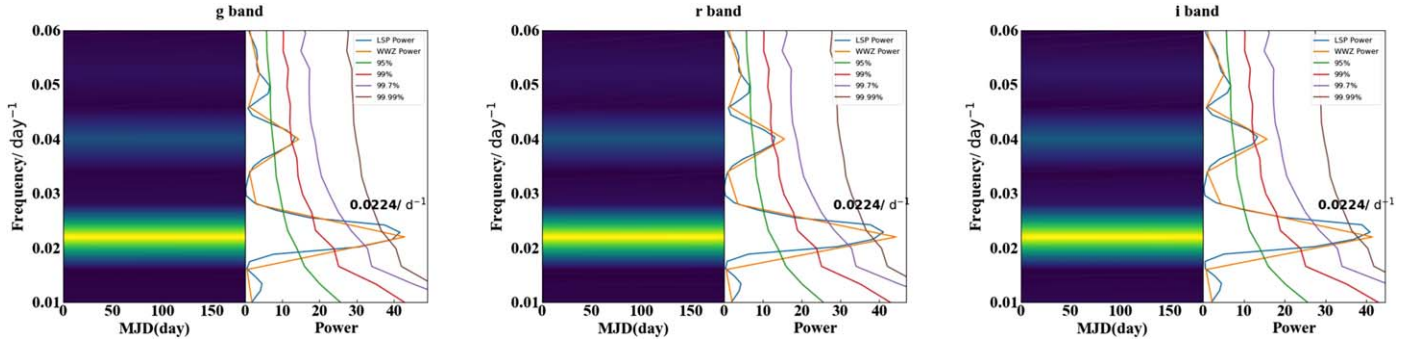

Figure 8. In the left panel, a color plot of the results of the WWZ method is shown (yellow is the strongest, and blue is the weakest). The analysis of the results of the WWZ and LSP methods is shown in the right panel, the coffee color curve represents the significance level of the curve at 99.99%, the purple curve represents the significance level of the curve at 99.7%, the red curve represents the significance level of the curve at 99%, and the green curve represents the significance level of the curve at 95%. The orange curve represents the time-averaged WWZ power, and the blue curve represents the LSP power. In the right panel, the highest peak is the position of periodic signals, which is about 0.0224 (1 day^{-1}), and its counterpart is a 44.6 day QPO with a significance level of 4.18σ.

ORCID iDs

Lin Lu https://orcid.org/0000-0002-0786-7307
Yunlu Gong https://orcid.org/0000-0003-3326-2173

References

Abdo, A. A., Ackermann, M., Agudo, I., et al. 2010, ApJ, 716, 30
Ackermann, M., Ajello, M., Albert, A., et al. 2015, ApJL, 813, L41
Ajello, M., Angioni, R., Axelsson, M., et al. 2020, ApJ, 892, 105
Aleksić, J., Ansoldi, S., Antonelli, L. A., et al. 2015, A&A, 576, A126
Angel, J. R. P., & Stockman, H. S. 1980, ARA&A, 18, 321
Bhatta, G. 2017, ApJ, 847, 7
Bhatta, G., & Dhital, N. 2020, ApJ, 891, 120
Bhatta, G., Zola, S., Stawarz, Ł., et al. 2016, ApJ, 832, 47
Biteau, J., & Giebels, B. 2012, A&A, 548, A123
Butuzova, M. S. 2021, APh, 129, 102577
Camenzind, M., & Krockenberger, M. 1992, A&A, 255, 59
Chen, J., Yi, T., Gong, Y., et al. 2022, ApJ, 938, 8
Edelson, R., Turner, T. J., Pounds, K., et al. 2002, ApJ, 568, 610
Emmanoulopoulos, D., McHardy, I. M., & Papadakis, I. E. 2013, MNRAS, 433, 907
Esposito, V., Walter, R., Jean, P., et al. 2015, A&A, 576, A122
Foster, G. 1996a, AJ, 111, 541
Foster, G. 1996b, AJ, 112, 1709
Goyal, A., Soida, M., Stawarz, Ł., et al. 2022, ApJ, 927, 214
Gupta, A. C., Srivastava, A. K., & Wiita, P. J. 2009, ApJ, 690, 216
Gupta, A. C., Tripathi, A., Wiita, P. J., et al. 2019, MNRAS, 484, 5785
Heidt, J., & Wagner, S. J. 1996, A&A, 305, 42
Hong, S. W., Xiong, D. R., & Bai, J. M. 2017, AJ, 154, 42
Hong, S. W., Xiong, D. R., & Bai, J. M. 2018, AJ, 155, 31
Horne, J. H., & Baliunas, S. L. 1986, ApJ, 302, 757
Iyida, E. U., Odo, F. C., Chukwude, A. E., & Ubachukwu, A. A. 2022, NewA, 90, 101666
Kapanadze, B. 2021, APh, 132, 102620
Li, X.-P., Cai, Y., Yang, H.-T., et al. 2021, MNRAS, 506, 1540
Li, X.-P., Yang, H.-Y., Cai, Y., et al. 2023, ApJ, 943, 157
Liu, X., Mi, L., Liu, B., & Li, Q. 2012, Ap&SS, 342, 465
Lomb, N. R. 1976, Ap&SS, 39, 447
Lu, L., Zhou, W.-L., Luo, G.-Y., & Sun, B. 2023, RAA, 23, 015012
Ma, L., Xie, G. Z., Zhou, S. B., et al. 2004, IJMPD, 13, 659
Nesci, R., Massaro, E., Rossi, C., et al. 2005, AJ, 130, 1466

Nilsson, K., Lindfors, E., Takalo, L. O., et al. 2018, A&A, 620, A185
Pininti, V. R., Bhatta, G., Paul, S., et al. 2023, MNRAS, 518, 1459
Prokhorov, D. A., & Moraghan, A. 2017, MNRAS, 471, 3036
Raiteri, C. M., Villata, M., Carosati, D., et al. 2021, MNRAS, 501, 1100
Raiteri, C. M., Villata, M., Tosti, G., et al. 2003, A&A, 402, 151
Rani, B., Gupta, A. C., Joshi, U. C., Ganesh, S., & Wiita, P. J. 2010, ApJL, 719, L153
Rani, B., Krichbaum, T. P., Fuhrmann, L., et al. 2013, A&A, 552, A11
Rejkuba, M., Minniti, D., & Silva, D. R. 2003, A&A, 406, 75
Ren, G. W., Ding, N., Zhang, X., et al. 2021a, MNRAS, 506, 3791
Ren, G. W., Zhang, H. J., Zhang, X., et al. 2021b, RAA, 21, 075
Rieger, F. M. 2019, Galax, 7, 78
Scargle, J. D. 1982, ApJ, 263, 835
Shah, Z., Mankuzhiyil, N., Sinha, A., et al. 2018, RAA, 18, 141
Shapiro, S. S., & Wilk, M. B. 1965, Biometrika, 52, 591
Sobacchi, E., Sormani, M. C., & Stamerra, A. 2017, MNRAS, 465, 161
Tripathi, A., Gupta, A. C., Aller, M. F., et al. 2021, MNRAS, 501, 5997
Urry, C. M., & Padovani, P. 1995, PASP, 107, 803
Uttley, P., McHardy, I. M., & Papadakis, I. E. 2002, MNRAS, 332, 231
Uttley, P., McHardy, I. M., & Vaughan, S. 2005, MNRAS, 359, 345
VanderPlas, J. T. 2018, ApJS, 236, 16
Vaughan, S. 2005, A&A, 431, 391
Vaughan, S., Edelson, R., Warwick, R. S., & Uttley, P. 2003, MNRAS, 345, 1271
Venters, T. M., Pavlidou, V., & Reyes, L. C. 2009, ApJ, 703, 1939
Vio, R., Andreani, P., & Biggs, A. 2010, A&A, 519, A85
Xie, G. Z., Liang, E. W., Zhou, S. B., et al. 2002, MNRAS, 334, 459
Xiong, D. R., Bai, J. M., Fan, J. H., et al. 2020, ApJS, 247, 49
Xiong, D. R., Bai, J. M., Zhang, H. J., et al. 2017, ApJS, 229, 21
Zhang, G. Q., Tu, Z.-L., & Wang, F. Y. 2021, ApJ, 909, 83
Zhang, P., & Wang, Z. 2022, ApJ, 934, 3
Zhang, P.-F., Yan, D.-H., Zhou, J.-N., et al. 2017, ApJ, 845, 82
Zhou, B., Dai, B. Z., & Yang, J. P. 2021, PASJ, 73, 850
Zhou, J. N., Wang, Z. X., Chen, L., et al. 2018, NatCo, 9, 4599
Zola, S., Valtonen, M., Bhatta, G., et al. 2016, Galax, 4, 41